Electronic Supplementary Material (ESI) for Journal of Materials Chemistry A.

Electronic Supplementary Information

Coordination-Enabled Synergistic Surface Segregation for Fabrication of Multi-defense Mechanism Membranes

Xueting Zhao[a,b], Yanlei Su[a,b], Heng Dai[a,b], Yafei Li[a,b], Runnan Zhang [a,b], Zhongyi Jiang[a,b,*]

[a] *Key Laboratory for Green Chemical Technology of Ministry of Education, School of Chemical Engineering and Technology, Tianjin University, Tianjin 300072, China*

[b] *Collaborative Innovation Center of Chemical Science and Engineering (Tianjin), Tianjin 300072, China*

---

[*] Corresponding author. School of Chemical Engineering and Technology, Tianjin University, No. 92, Weijin Road, Nankai District, Tianjin 300072, China

Tel: 86-22-27406646. Fax: 86-22-27406646.

E-mail address: zhyjiang@tju.edu.cn (Z.Y. Jiang)

S1. Experimental Materials and Methods

S1.1 Materials

PVDF (FR-904) was purchased from Shanghai 3F New Material Co. Ltd and dried at 110 ^{o}C for 12 h before use. 2,2,3,4,4,4-hexafluorobutyl acrylate (HFBA) purchased from Xeogia Fluorine-Silicon Chemical Co. Ltd. was washed twice with a sodium hydroxide solution (1 mol/L) and deionized water. Acrylic acid (AA) was purchased from Heowns Biochem Technologies LLC. Titanium (IV) butoxide (TBT), 2,2'-azobis(2-methylpropionitrile) (AIBN), n-butylmethacrylate (BMA), absolute ethanol, N-methylpyrrolidinone (NMP), sodium dodecylsulfate (SDS), n-heptane, n-hexadecane, silicone oil were purchased from Tianjin Guangfu Fine Chemical Research Institute. High-speed vacuum pump oil (GS-1) was purchased from Beijing Sifang Special Oil Factory. Soybean oil was purchased from a local food store. Bovine serum albumin (BSA) was purchased from Tianjin Lianxing Biological Agent Company. All the above materials were used as received unless otherwise stated.

S1.2 Synthesis of Amphiphilic PHFBA-xPAA Copolymers

The radical polymerization of PHFBA-xPAA copolymers was carried out via sequential monomer addition. First, HFBM monomer (2.36 g, 10 mmol) was polymerized in ethanol (40 mL) using molar ratios of [HFBM]/[AIBN]=20:1 under nitrogen at 70 ^{o}C. After 2 h, the mixture of the AA monomer (5 mmol, 10 mmol, 20 mmol or 30 mmol) and ethanol (10 mL) purged with N_2, was added dropwise to the reaction solution. Polymerization was performed for another 8 h and then terminated by cooling and exposing to air. The resulting product was purified by precipitating into n-hexane for three times and then dried by freeze drying for 12 h to yield white solid. The compositions and molecular weights determined by ^{1}H nuclear magnetic resonance (^{1}H NMR, Varian Inova 500) method were summarized in Table S1. The nomenclature PHFBA-xPAA (x=0.5, 1, 2, and 3) was used for synthesized copolymers where the indices x indicated the molar ratio of HFBA to AA units. PBMA-2PAA copolymer was also synthesized for further use.

S1.3 Membrane Preparation and Characterizations

The TiO_2 hybrid membranes were fabricated by combining the non-solvent induced phase inversion and in situ sol-gel processes. PVDF and PHFBA-xPAA were dissolved in NMP (dried over 4A molecular sieves), respectively, to form homogenous solutions (PVDF/NMP and PHFBA-xPAA/NMP). Given quantities of TBT were slowly added dropwise into PHFBA-xPAA/NMP solutions with rapid stirring. After stirring for 12 h at 60 ^{o}C, the solutions turned gradually to dark orange (see Fig. S3). Then, the PHFBA-xPAA/TBT/NMP solutions were added dropwise into PVDF/NMP solutions and stirred for 12 h at 60 ^{o}C to form homogeneous and transparent casting solution. The final concentrations of PVDF and PHFBA-xPAA were consistent with the above casting solutions: 16.0 and 8.0 wt%, respectively. The calculated amount of TiO_2 NPs was 1, 3 and 5 wt% *versus* the weight of PVDF. Afterwards, the casting solutions were degassed for another 12 h. After releasing air bubbles, the casting solutions were cast onto a glass plate using a casting knife with a gap height of 240 μm and immersed immediately in a 25 ^{o}C non-solvent (water) bath. After detachment, the membranes were removed and stored in deionized water before use. (Note that the viscosity of casting solutions with even higher TBT addition was too high for membrane casting.)

PVDF/PEG membrane was prepared as control membranes from the casting solution containing PVDF (16 wt%) and PEG2000 (8 wt%, pore-forming agent). PVDF/PHFBA/TiO_2 membrane with calculated amount of 5 wt% TiO_2 NPs (*versus* PVDF) and PVDF/PBMA-2PAA polymeric membrane were prepared for further comparison.

Scanning electron microscopy (SEM, FEI Nova Nanosem 430) was used to inspect the surface and cross-section morphologies of membranes. Atomic force microscopy (AFM, Multimode 3, Bruker) was used to analyze the surface morphologies and surface roughness of membranes. X-ray photoelectron spectroscopy (XPS, Kratos Axis Ultra DLD) and attenuated total reflection Fourier transform infrared spectroscopy (ATR-FTIR, Nicolet 6700) were used to analyze the chemical feature of membrane surfaces. Diffuse reflection UV-Vis spectrophotometer (DR-UV/Vis, Hitachi U-3010) were used to determine the interaction within composite SSS. Thermogravimetric analysis (TGA, NETZSCH TG209 F3, air atmosphere) equipment and ^{1}H NMR were used to determine the bulk compositions in hybrid membranes. Differential scanning calorimetry (DSC, Netzsch DSC 200F) was used to analyze the states of water in the hybrid membrane samples (After removing surplus water by filter paper, each DSC sample sealed in Al pan was first cooled to -40 ^{o}C, and then heated to 40 ^{o}C at a scanning rate of 5 ^{o}C/min). Tensile testing machine (Testometric AXM350-10KN) was applied to determine mechanical properties of membranes. Transmission electron microscope (TEM, JEM-2100F) was used to observe the morphology of the generated TiO_2 NPs after removing organic matters by calcination. Contact angle goniometer (JC2000C Contact Angle Meter) was used to investigate the contact angles of membrane surface from water (or diiodomethane) sessile drop (5 μL) and air (or oil) captive bubble (10 μL) in water. Each membrane was exposed to water for at least 24 h prior to underwater contact angle measurements. The total (γ_s), polar (γ_s^p) and dispersive (γ_s^d) surface energy of membrane surfaces was calculated from the Owens and Wendt's method [1] employing a polar test liquid (water) and a nonpolar test liquid (diiodomethane).

$$\gamma_S = \gamma_S^d + \gamma_S^p \qquad \text{(S1)}$$

$$(1+\cos\theta)\gamma_L = 2(\gamma_L^d \gamma_S^d)^{1/2} + 2(\gamma_L^p \gamma_S^p)^{1/2} \qquad \text{(S2)}$$

S1.4 Oil/Water Filtration and Antifouling Property Evaluation

A dead-end stirred cell with effective membrane area of 28.7cm^2 was employed to evaluate the filtration and antifouling properties of hybrid membranes for oil/water separation. The transmembrane pressure was controlled by pressurized nitrogen gas. The operation pressure and stirring speed were locked at 0.05 MPa and 200 rpm, respectively. The pure water flux J_{w1} (L/(m^2 h)) of each membrane was recorded after pressurized for 1 h (until reaching the steady value) and calculated by the following formula:

$$J_{w1} = \frac{V}{A\Delta T} \tag{S3}$$

where V (L) is the permeated water volume, A (m^2) is the effective membrane area and ΔT (h) is the operation time. For antifouling property evaluation, oil-in-water emulsion (GS-1 high-speed vacuum oil 0.9 g L^{-1} and SDS 0.1 g L^{-1}, average diameter ~2.1μm) was employed as the model foulant solution. The membrane was subsequently filtrated with oil-in-water emulsion for 1 h and the flux for feed solutions (J_p) was recorded and calculated in the same manner. After the filtration of oil-in-water emulsion, the membrane was cleaned with water for 30 min and the flux of cleaned membrane (J_{w2}) was recorded and calculated according to the first step. Membrane antifouling properties, including inhibition of flux decline and improvement of flux recovery, were analyzed in detail by introducing several parameters: total flux decline ratio (DR_t=1-J_p/J_{w1}), reversible flux decline ratio (DR_r=(J_{w2}-J_p)/J_{w1}), irreversible flux decline ratio (DR_{ir}=1-J_{w2}/J_{w1}), and flux recovery ratio (FRR=J_{w2}/J_{w1}). Generally, higher flux recovery and lower flux decline indicated better antifouling properties of membranes and separation performance for oil/water separation.

S2. Characterization of Amphiphilic Copolymers

Table S1 Characterization of PHFBA-xPAA copolymers.

Sample ID	Copolymer compositions (mol %)	
	HFBA: AA [a]	M_n (kg/mol) [b]
PHFBA-0.5PAA	1:0.55	10.6
PHFBA-PAA	1:0.95	11.4
PHFBA-2PAA	1:1.96	14.6
PHFBA-3PAA	1:3.09	16.8

[a] Copolymer compositions calculated from ^{1}H NMR spectra in dimethyl sulfoxide-d6. [b] Mn of the copolymers determined by ^{1}H NMR spectra.

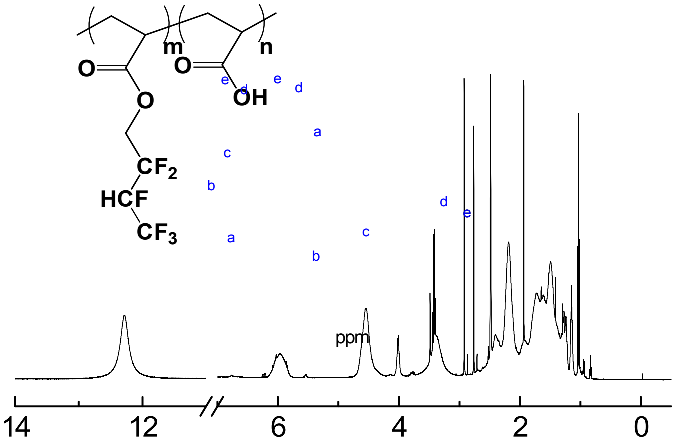

Fig. S1 ^{1}H NMR spectra of PHFBA-2PAA copolymers with different synthesis formulations. *m* represents the degree of polymerization (DP) of HFBA mononer. *n* represents the degree of polymerization (DP) of AA mononer. From the integrations of methylene proton signal (PHFBA) at 4.55 ppm and carboxylic acid signal at 12.3 ppm, the ratio of n/m was calculated as 1.96, which was close to the feed ratio of the monomers in synthesis formulations.

S3. Preparation, Surface Property and Antifouling Performance of PVDF/PHFBA-xPAA Membranes

PVDF/PHFBA-xPAA membranes were fabricated by non-solvent induced phase inversion process. PVDF (16 wt%) and PHFBA-xPAA copolymers (8 wt%) were dissolved in NMP (dried over 4A molecular sieves). After mixed by stirring for 12 h at 60 ^{o}C, the casting solutions were degassed for another 12 h. After releasing air bubbles, the casting solutions were cast onto a glass plate using a casting knife with a gap height of 240 μm and immersed immediately in a 25 ^{o}C water bath. After detachment, the membranes were removed and stored in deionized water before use.

As an *in situ* approach to membrane surface modification, surface segregation of amphiphilic copolymers coupled with the wet phase inversion process has been adopted to generate efficacious brushes on membrane surfaces [2]. The characterization of PVDF/PHFBA-xPAA membranes was carried out to provide insight into surface segregation behavior of PHFBA-xPAA copolymers. The detailed information of PHFBA-xPAA copolymers was summarized in Table S1.

As shown in Fig. S2a, the surface PHFBA and PAA compositions, calculated from XPS signal intensities and differentiation (Fig. S2b), was obviously higher than both the bulk and the membrane casting solution compositions of PHFBA and PAA segments. This obvious difference manifested the “free surface segregation” of hydrophilic PAA segments and “forced surface segregation” of low surface energy PHFBA segments during phase inversion process, as confirmed in previous study [3]. Hydrophilic PAA segments spontaneously segregated to cover membrane-water interface driven by hydration ability of PAA segments, and impaired entropic driving force for the migration of low surface energy PHFBA segments toward membrane-water interface. As the PAA fraction in the chains of copolymers was increased, the gradual increase of surface PAA composition was consistent with the increasing tendency of bulk PAA composition. Additionally, higher PAA fraction in the chains of copolymers finally accelerated the leaching of PHFBA-3PAA copolymers out of the blend membranes (lower bulk composition than membrane casting solution composition) and induced the ultimate decrease in surface PAA composition. Unlike the gradual decrease in bulk PHFBA composition, the surface PHFBA composition were first increased and then decreased as the PHFBA fraction in the chains of copolymers was decreased. This interesting transition was attributed to the synergistic effect during PVDF/PHFBA-xPAA membrane formation: on one hand, the surface enrichment of hydrophilic PAA segments to minimize interfacial energy promoted the forced surface segregation behavior of PHFBA segments and led to the remarkable increase of PHFBA segments; On the other hand, the further decrease in PHFBA fraction in the chains of copolymers and the increased leaching amount induced the subsequent decrease in surface composition of PHFBA segments.

The variations in static water contact angles (CA_w) and total surface energies (γ_s) underwent the similar change tendency as surface composition of PHFBA segments (Fig. S2c). For detailed surface energy analysis, the variation in polar surface energies (γ_s^p) was coincident with the changing trend in surface composition of polar PAA segments, and the variation in dispersive surface energy (γ_s^d) showed an obvious switch from decreasing to increasing, which was coincident with the change in the surface composition of nonpolar PHFBA segments. The membranes with lower surface energy were assumed to be unfavorable for oil fouling and diffusion, and the changes in membrane antifouling parameters were presented in Fig. S2d. PVDF/PHFBA-2PAA membrane exhibited the lowest flux decline and the highest flux recovery due to optimization of mixed brush architecture which combined the fouling-resistant ability of hydrophilic PAA segments and the fouling-release ability of low surface energy PHFBA segments. Similar phenomena were also observed on heterogeneous membrane surfaces reported in our previous studies [3-4].

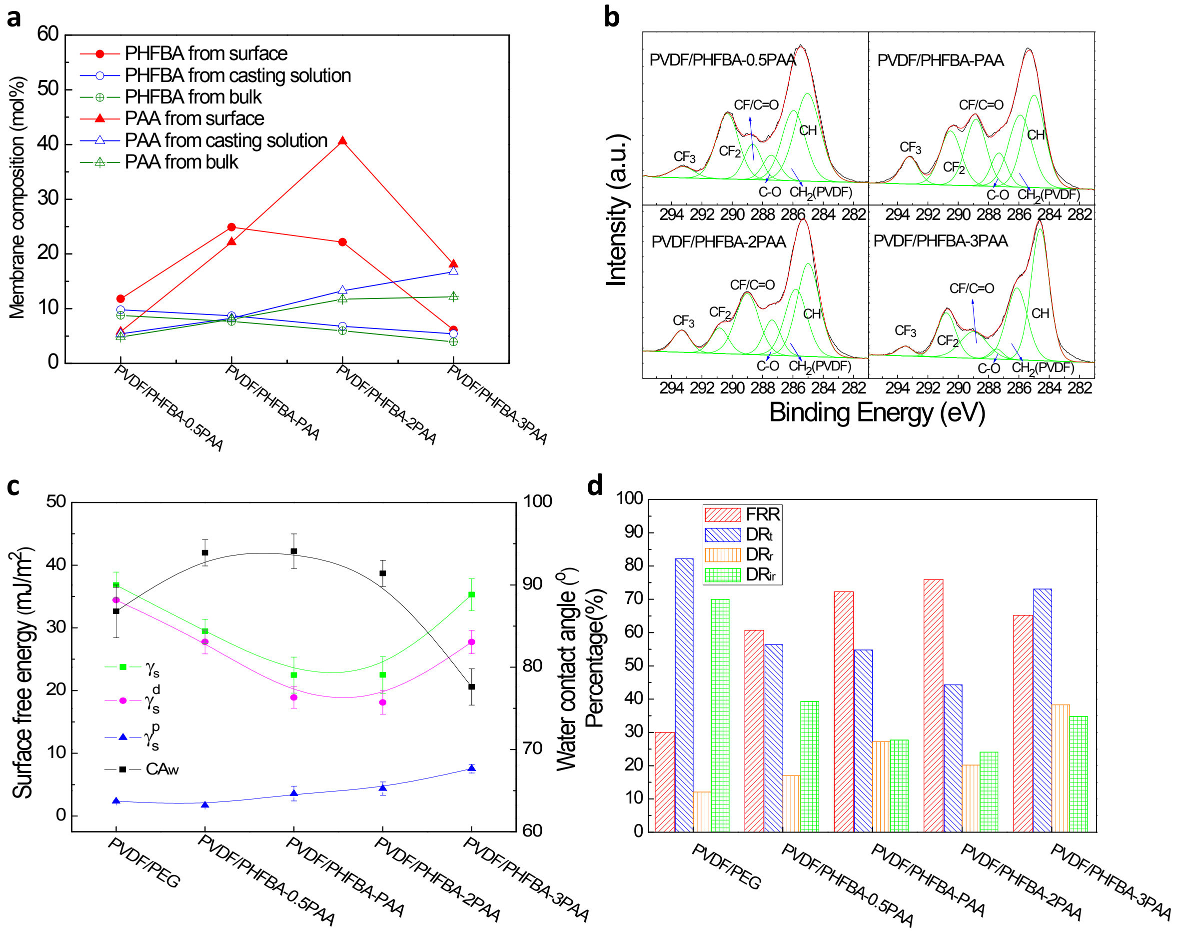

Fig. S2 (a) The surface compositions, bulk compositions, and casting solution composition of PHFBA and PAA segments for PVDF/PHFBA-xPAA membrane. (b) C1s XPS spectra of PVDF/PHFBA-xPAA membranes split into six peaks corresponding to neutral $\underline{\mathrm{C}}\mathrm{H}$ at 285.0 eV, $\underline{\mathrm{C}}\mathrm{H}_2$(PVDF) at 285.9 eV, $\underline{\mathrm{C}}$-O at 287.6 eV, $\underline{\mathrm{C}}$=O($\underline{\mathrm{C}}$-F) at 288.9 eV, $\underline{\mathrm{C}}\mathrm{F}_2$ at 290.8 eV, $\underline{\mathrm{C}}\mathrm{F}_3$ at 293.5 eV. (c) Water contact angles (sessile drop) and the surface free energy parameters including γ_s, γ_s^d and γ_s^p of PVDF/PHFBA-xPAA membranes. (d) Membrane antifouling parameters of PVDF/PHFBA-xPAA membranes during oil-in-water emulsion filtration including *FRR*, DR_t , DR_r, DR_{ir}.

S4. Coordination Interaction between Titanium(IV) and PHFBA-xPAA

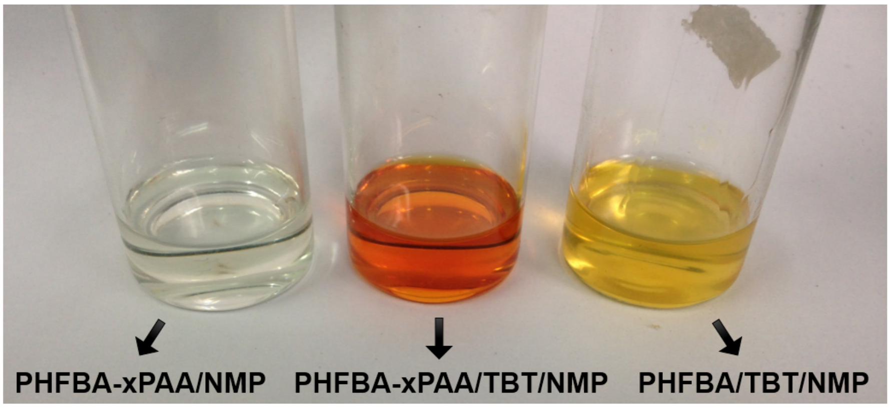

Fig. S3 Photos of the PHFBA-xPAA solution before and after complexing with Ti(IV).

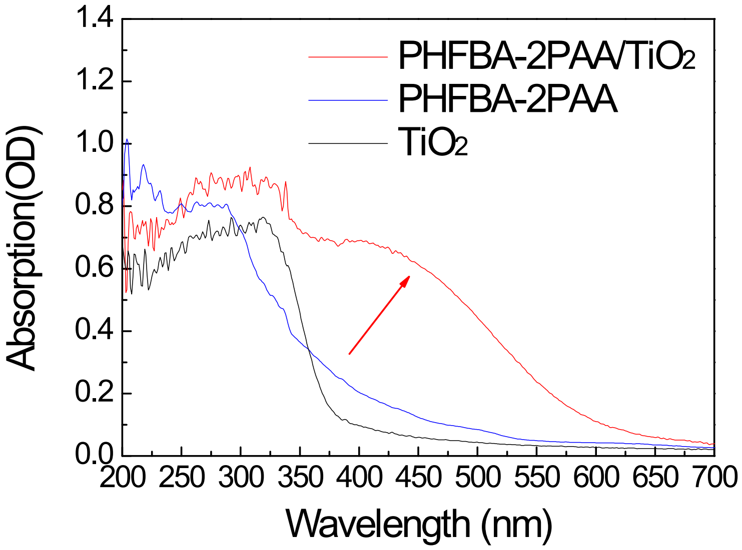

Fig. S4 DR/UV–vis spectra of TiO_2, PHFBA-2PAA and PHFBA-2PAA/TiO_2. It was noticed that the absorption of PHFBA-2PAA copolymer was obviously shifted to lower energy. The red-shift and increase in the width of PHFBA-2PAA absorption could be ascribed to the coordination interactions between PHFBA-2PAA and TiO_2 NPs.

S5. Morphologies and Mechanical Strength of Hybrid Membranes

The as-prepared hybrid membranes fabricated by non-solvent induced phase inversion process displayed typically skinned asymmetric morphology. The cross-section and top-surface morphologies of the PVDF, PVDF/PHFBA-2PAA and PVDF/PHFBA-2PAA/TiO_2 hybrid membranes were observed using SEM (Fig. S5). Similar to typical pore-forming agent PEG, amphiphilic copolymer PHFBA-2AA would help the diffusion of the solvent and the non-solvent, and facilitate the porous structure formation. The asymmetric morphologies of membranes with top skin layers supported by finger-like microvoids were affected by the TiO_2 content in polymer blends. In case of PVDF/PHFBA-2PAA/TiO_2 hybrid membranes, the generated hydrophilic TiO_2 NPs would accelerated the diffusion of solvent and non-solvent during phase inversion, thus favored the elongation of finger-like microvoids beneath the skin layers across the thickness. Furthermore, the PVDF/PHFBA-2PAA/TiO_2 hybrid membranes showed the decrease of large macrovoids at the bottom with increasing TiO_2 content. The generation of macrovoids was triggered liquid-liquid phase separation and the growth of the macrovoids was affected by rheological property of the casting solution [5]. Considering that the viscosity of casting solutions were increased with the feed TBT content increasing (see Table S2), the suppression of large macrovoid formation was probably due to rheological hindrance. The decrease in the observable pore size and the increase in the porosity on hybrid membrane surfaces were also observed in Fig. S5c-e. The decreased pore size could be tentatively interpreted by the limited phase separation kinetics of PHFBA-2PAA copolymer in PVDF matrix due to the attachment of carboxylic groups on TiO_2 surface. The membrane effective pore sizes calculated from BSA rejection (see Table S2) also suggested a better agreement with the pore size variation from SEM observations. The increased porosity was explained by the interfacial stresses between polymer and TiO_2 NPs arisen from the different shrinkage rates of organic phase and inorganic TiO_2 phase during phase inversion process [6]. The SEM images also demonstrated that no TiO_2 nanoparticle aggregation could be observed in all the hybrid membranes. The coordinated amphiphilic copolymer would reduce the attractive interactions between TiO_2 nanoparticles (NPs) and confer favorable entropy of mixing with the matrix polymer, yielding good dispersion at molecule level [7] and high mechanical strength (Fig. S6). The decreased pore size and good dispersion of TiO_2 NPs also contributed to the decreased surface roughness (see Fig. S5, three-dimensional AFM images). The typical asymmetric finger-like structure, smaller pore size, higher porosity, and remarkably improved membrane mechanical strength, endowed the as-prepared hybrid membranes with the outstanding ability of selective separation.

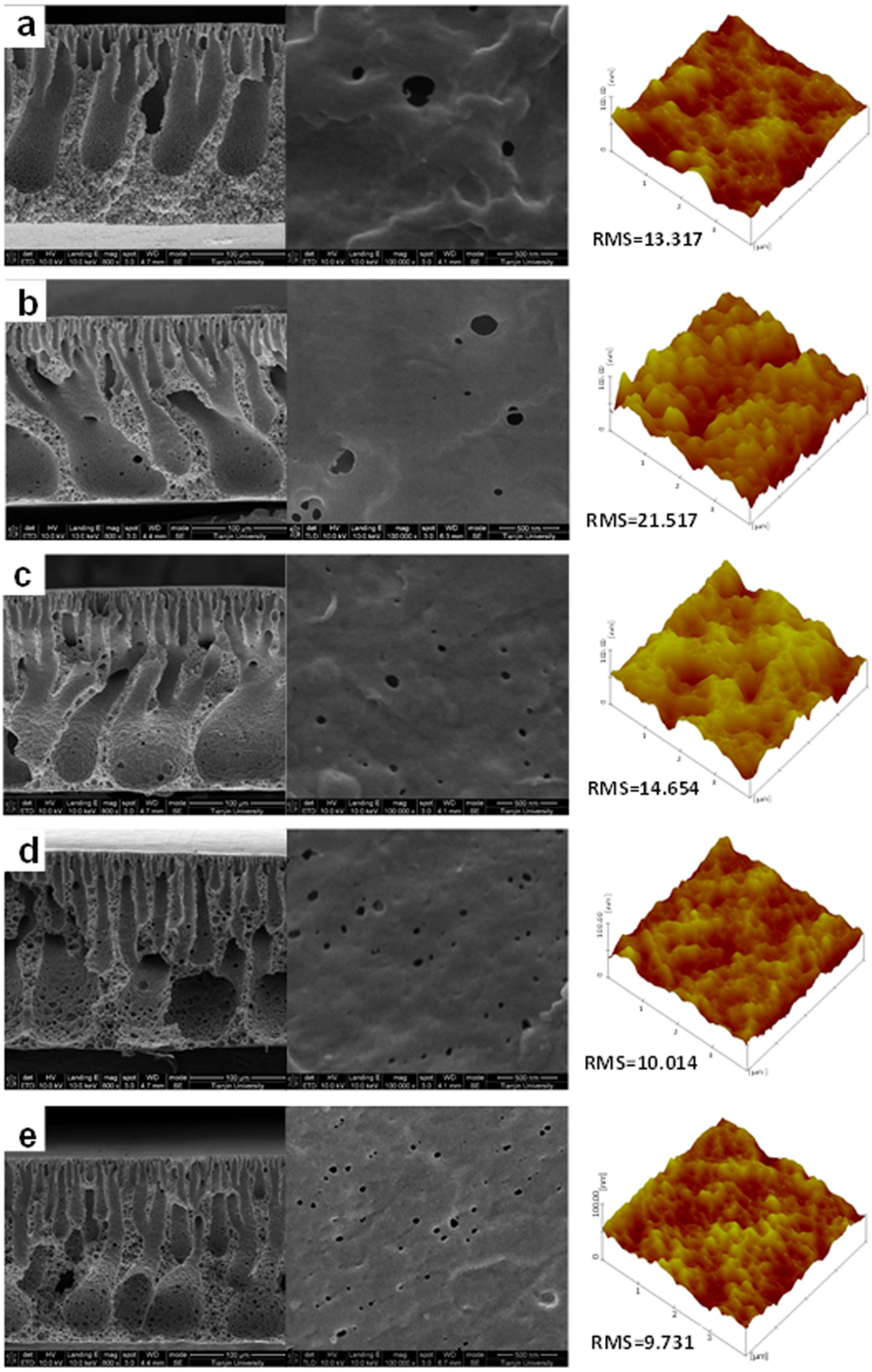

Fig. S5 Cross-section SEM images (left) and top surface SEM (middle) and AFM (right) images of (a) PVDF/PEG control membrane, (b) PVDF/PHFBA-2PAA membrane, and PVDF/PHFBA-2PAA/TiO_2 hybrid membranes with calculated TiO_2 amount of (c) 1 wt%, (d) 3 wt%, and (e) 5 wt%.

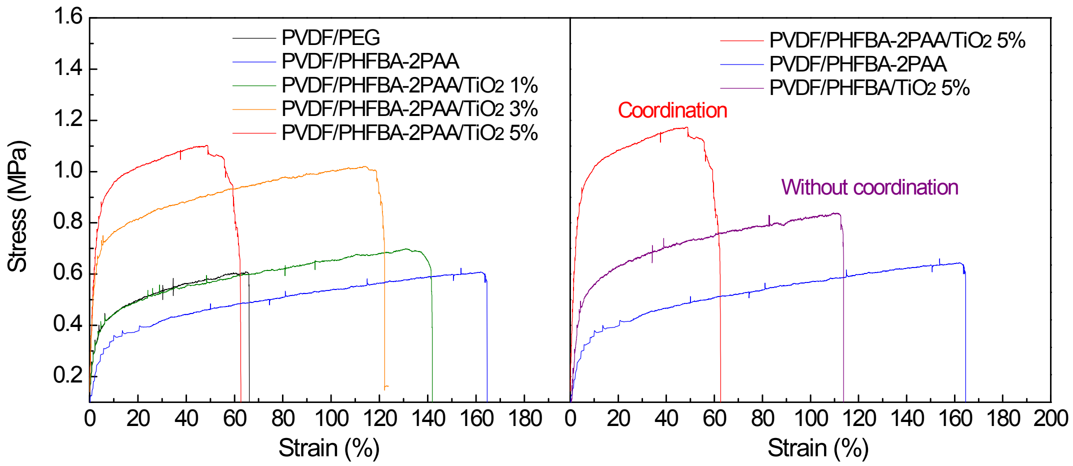

Fig. S6 Stress-strain curves of PVDF/PEG, PVDF/PHFBA-2PAA, PVDF/PHFBA-2PAA/TiO_2 hybrid membranes and the effect of coordination interaction between PAA and TiO_2 NPs. The Young's modulus and ultimate tensile strength of PVDF/PHFBA-2PAA/TiO_2 5% membrane were increased by 650% and 72% respectively as compared to PVDF/PHFBA-2PAA membrane. The hybrid membranes with coordination interactions between PHFBA-2PAA and TiO_2 exhibited the best mechanical property compared with those without coordination or hybridization.

Table S2 Viscosity of membrane casting solutions, effective pore sizes and oil rejection of membranes.

Membranes	Viscosity (mPa·s) [a]	Pore size (nm) [b]	Oil rejection (%) [c]
PVDF/PEG	1224	51.8	>99.9%
PVDF/PHFBA-2PAA	1453	46.6	>99.9%
PVDF/PHFBA-2PAA/TiO_2 1%	1780	12.0	>99.9%
PVDF/PHFBA-2PAA/TiO_2 3%	2788	11.2	>99.9%
PVDF/PHFBA-2PAA/TiO_2 5%	3867	10.2	>99.9%

[a] Brookfield viscometer model DV-I Prime was used to determine the viscosity of the casting

solution at 25 °C. The casting solution of PVDF/PHFBA-2PAA/TiO_2 7% has viscosity of 4733 mPa·s. [b] The effective pore size of membranes was calculated from the formula developed by Zeman and Wales [8] using BSA as the model protein: $R = 1 - (1-\lambda)^2 \cdot \left[2 - (1-\lambda)^2\right] e^{-0.7146\lambda^2}$, where R is the rejection of BSA determined by UV-spectrophotometer (UV-9200) and λ is the ratio of BSA radius to pore radius. The hydrodynamic radius of BSA was taken as 3.5nm [9]. [c] The oil rejections were calculated from the oil concentration analyzed by UV-spectrophotometer (531 nm) in the feed and permeate solutions, respectively.

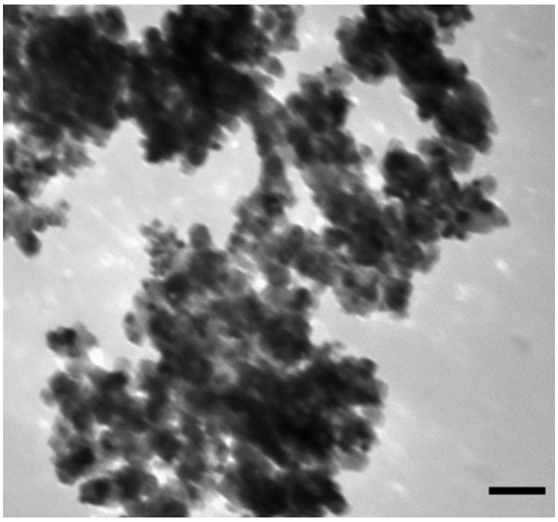

Fig. S7 TEM image of generated TiO_2 nanoparticles in hybrid membranes (scale bar, 200 nm).

S6. Wetting Behavior of Membrane Surfaces in Different Environments

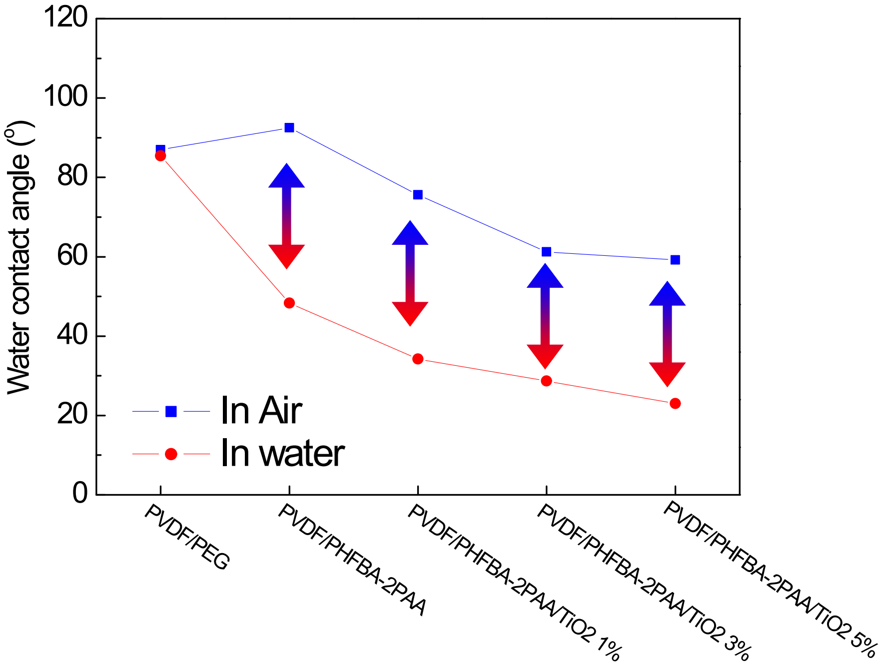

Fig. S8 The water contact angles of PVDF/PEG, PVDF/PHFBA-2PAA, and PVDF/PHFBA-2PAA/TiO_2 hybrid membranes in air and water environments. (The underwater water contact angle was the supplementary angle of the captive contact angle of an air bubble.)

The resultant surface heterogeneousity from PHFBA segments, PAA segments and TiO_2 NPs significantly influenced the wetting behavior of membrane surfaces (Fig. S8). The water contact angles in air environment were first increased then decreased when adjusting the mass ratio of PHFBA-2PAA copolymer and TiO_2 NPs. The water contact angle of PVDF membrane surface was about 86.9°. For PVDF/PHFBA-2PAA membrane, the water contact angle was slightly increased to about 92.5°. The increase can be attributed to the synergistic effect of surface enriched low surface energy PHFBA segments and hydrophilic PAA segments. Subsequent TiO_2 *in situ* hybridization enhanced the surface hydrophilicity remarkably and decreased water contact angle to about 57.3°. It was also found that the underwater water contact angles of PVDF/PHFBA-2PAA and PVDF/PHFBA-2PAA/TiO_2 hybrid membranes were significantly lower than the corresponding water contact angles measured in air environment. Because the heterogeneous surfaces usually possessed the capability of dynamic conformational response to environmental changes, the obvious differences in the surface wettability should be ascribed to the surface reconstruction triggered by exposure to different environments [10].

S7. Stability Test for Hybrid Membranes

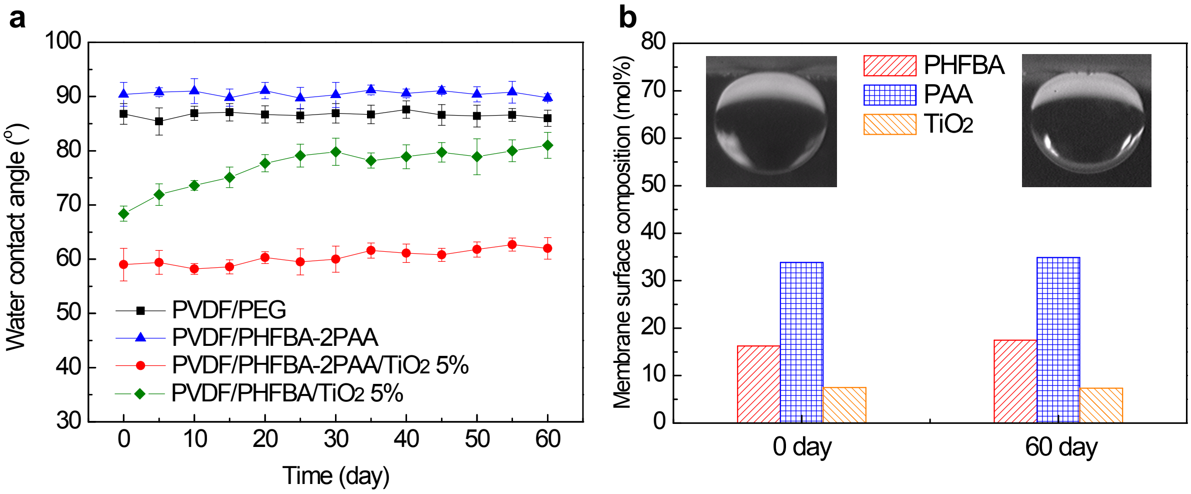

Fig. S9 (a) The variation in initial water contact angles of PVDF/PEG, PVDF/PHFBA-2PAA, and PVDF/PHFBA-2PAA/TiO_2 5% membranes with water immersion time (using sessile drop method). (b) The comparison of actual surface composition on PVDF/PHFBA-2PAA/TiO_2 5% membrane surface before and after 60-day immersion (determined by XPS analysis). The inset is photographs of underwater hexadecane captive bubbles before and after 60-day immersion.

Considering the potential practical application, the stable fixation of SSSs was a critical issue for membranes prepared by the above-proposed synergistic surface segregation. After 60-days immersion, the PVDF/PHFBA-2PAA/TiO_2 5% membrane still exhibited stable surface composition, water contact angle, and underwater hexadecane antiwetting behavior, revealing the excellent stability of PVDF/PHFBA-2PAA/TiO_2 hybrid membrane. The excellent stability could be interpreted by the strong coordination between Ti(IV) complex and PAA as well as the favorable self-healing ability of inside-stored SSSs in proximity to the surfaces programmed via surface reconstruction.

S8. DSC Studies on Water State in Hybrid Membranes

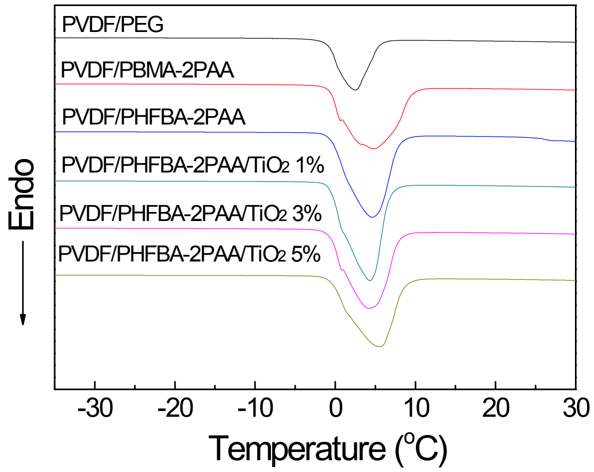

Fig. S10 DSC heating thermograms of PVDF/PEG, PVDF/PHFBA-2PAA, and PVDF/PHFBA-2PAA/TiO_2 hrbrid membranes. The enthalpy of fusion of free water was observed at about 2.5 ^{o}C and the complex broad endothermic peaks for the membranes were mainly due to the freezing bound water. The amount of total water was calculated from $(m_{\text{wet membrane}}-m_{\text{dry membrane}})/m_{\text{wet membrane}}\times 100\%$. The amount of free water (unbound water and freezing bound water) was calculated from the ΔH values, assuming melting of ice has ΔH = 334.45 J/g. The amount of bound water was calculated by subtracting the amount of free water from the total water content.

A deeper understanding of the water states of PVDF/PHFBA-2PAA/TiO_2 hybrid membranes was essential to elucidate the combined hydration ability of PAA segments and TiO_2 NPs (Table 2 and Fig. S10). Since most of PEG molecules leached out during phase inversion process, the hydrophobic PVDF/PEG membrane could hold only small amount of bound water due to the lack of hydrophilic segments. In contrast, both PVDF/PBMA-2PAA and PVDF/PHFBA-2PAA contained more bound water about 2.4 wt.%. The hydration ability was enhanced by electrostatic interaction between PAA segments and water molecules in the environment [11]. The pronounced increase of bound water in membrane (from 2.4 wt.% to 6.5 wt.%) was achieved based on the hybridization of

TiO_2 NPs capable of forming hydrogen bonds on the hydrophilic nanoparticle surfaces [12]. The synergistic effect of PAA segment and TiO_2 NPs were critical to maintain water molecules tightly bounded, leading to compact hydration layer and high hydrophilicity on membrane surfaces.

S9. Antifouling Performance of Membranes from Single-defense and Multi-defense Mechanisms

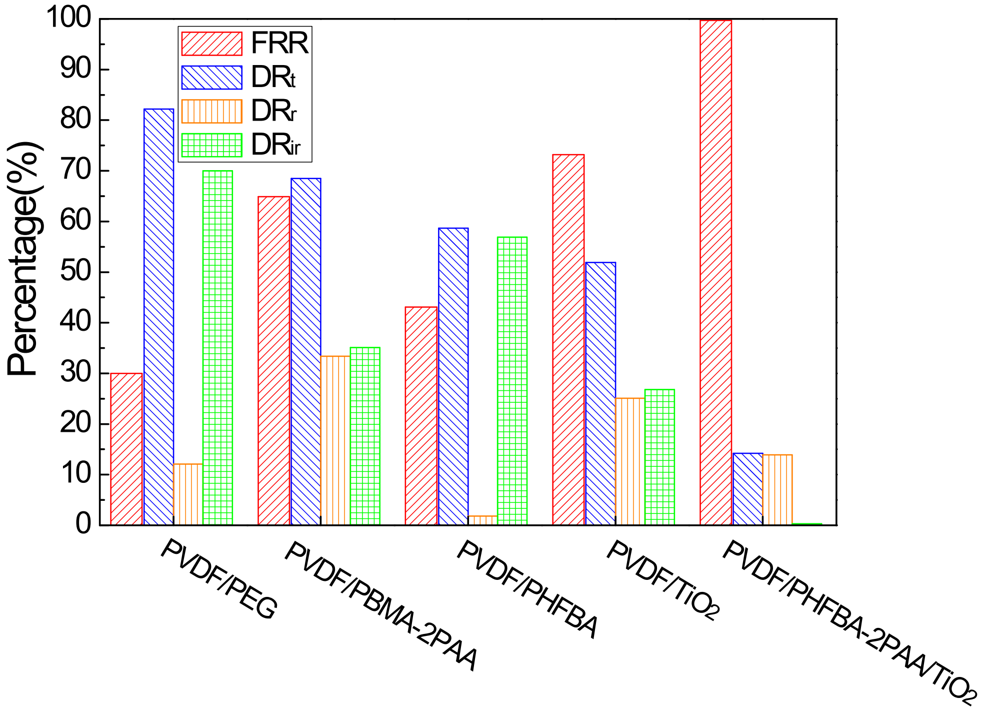

Fig. S11 A summary of the corresponding fouling parameters of membranes based on single- and multi-defense mechanism, including *FRR*, DR_t, DR_r, and DR_{ir}. PVDF/PBMA-2PAA was in accordance with antifouling membranes derived from PAA-based fouling-resistant defense mechanism. PVDF/PHFBA was in accordance with antifouling membranes derived from PHFBA-based fouling-release defense mechanism. PVDF/TiO_2 was in accordance with antifouling membranes derived from TiO_2-based fouling-resistant defense mechanism. PVDF/PHFBA-2PAA/TiO_2 membrane was in accordance with antifouling membranes based on multi-defense mechanism.

S10. Calculation formula of the surface compositions of PAA segments, PHFBA segments and TiO2 NPs on membrane surfaces

The atom percentage of C from $-CF_3$ groups in PHFBA segments,

$$A_{CF3}=\Phi_{CF3}\times C\% \tag{S4}$$

The atom percentage of C from -C=O and -CFH groups in PHFBA segments,

$$A_{CF/C=O(PHFBA)}=2\times A_{CF3} \tag{S5}$$

The atom percentage of C from -C=O groups in PAA segments,

$$A_{C=O(PAA)}=\Phi_{CF/C=O}\times C\%-A_{CF/C=O(PHFBA)} \tag{S6}$$

The atom percentage of C from $-CH_2$(PVDF) groups in PVDF,

$$A_{CH2(PVDF)}=\Phi_{CH2(PVDF)}\times C\% \tag{S7}$$

The atom percentage of Ti in TiO_2,

$$A_{Ti}=Ti\% \tag{S8}$$

where C% and Ti% was the atom percentage of C and Ti elements on membrane surfaces determined by XPS. Φ was the area ratio of the different peaks in C 1s XPS spectra. The factor 2 accounted for the two C atoms from -C=O and -CFH groups in per repeat unit of HFBA side chains with one C atoms from $-CF_3$ group. Since there was one $-CF_3$ group, -C=O group, Ti atom and $-CH_2$ group in each unit of HFBA, AA, TiO_2 and PVDF, respectively, the molar percentages (M_x) of HFBA, AA and TiO_2 could be calculated readily as:

$$M_x=\frac{A_x}{A_{CF3}+A_{C=O(PAA)}+A_{Ti}+A_{CH2(PVDF)}}\times 100\% \tag{S9}$$

[1] D. K. Owens, R. C. Wendt, *J. Appl. Polym. Sci.* **1969**, *13*, 1741-1747.

[2] M. A. Shannon, P. W. Bohn, M. Elimelech, J. G. Georgiadis, B. J. Marinas, A. M. Mayes, *Nature* **2008**, *452*, 301-310.

[3] W. Chen, Y. Su, J. Peng, Y. Dong, X. Zhao, Z. Jiang, *Adv. Funct. Mater.* **2011**, *21*, 191-198.

[4] X. Zhao, W. Chen, Y. Su, W. Zhu, J. Peng, Z. Jiang, L. Kong, Y. Li, J. Liu, *J. Membr. Sci.* **2013**, *441*, 93-101.

[5] M.-J. Han, S.-T. Nam, *J. Membr. Sci.* **2002**, *202*, 55-61.

[6] Y. Yang, H. Zhang, P. Wang, Q. Zheng, J. Li, *J. Membr. Sci.* **2007**, *288*, 231-238.

[7] N. Jouault, D. Lee, D. Zhao, S. K. Kumar, *Adv. Mater.* **2014**, *26*, 4031-4036.

[8] L. Zeman, M. Wales, *Polymer Solute Rejection by Ultrafiltration Membranes, Vol. 154*, American Chemical Society, Washington, DC, USA, **1981**.

[9] K. B. Kosto, W. M. Deen, *AIChE J.* **2004**, *50*, 2648-2658.

[10] T. P. Russell, *Science* **2002**, *297*, 964-967.

[11] M. Kobayashi, Y. Terayama, H. Yamaguchi, M. Terada, D. Murakami, K. Ishihara, A. Takahara, *Langmuir* **2012**, *28*, 7212-7222.

[12] G. Li, L. Li, J. Boerio-Goates, B. F. Woodfield, *J. Am. Chem. Soc.* **2005**, *127*, 8659-8666.